Schweizerische Eidgenossenschaft
Confédération suisse
Confederazione Svizzera
Confederaziun svizra

Eidgenössisches Departement für
Umwelt, Verkehr, Energie und Kommunikation UVEK

Bundesamt für Energie BFE

Jahresbericht 27. November 2009

Development and modelling of a Thermoelectric Oxide Module (TOM) as demonstrator

Auftraggeber:
Bundesamt für Energie BFE
Forschungsprogramm Elektrizitätstechnologien & -anwendungen
CH-3003 Bern
www.bfe.admin.ch

Auftragnehmer:
EMPA Dübendorf
Überlandstrasse 129
CH-8600 Dübendorf
www.empa.ch/abt131

Autoren:
Petr Tomes, EMPA, Petr.Tomes@empa.ch
Anke Weidenkaff, EMPA, Anke.Weidenkaff@empa.ch

BFE-Bereichsleiter: Dr. Michael Moser
BFE-Programmleiter: Roland Brüniger
BFE-Vertrags- und Projektnummer: 152820 / 101356

Abstract

The thermoelectric conversion of heat into electricity at high temperatures is impossible with conventional converters. Thus, a high temperature stable demonstrator is developed to convert concentrated solar radiation directly into electricity at high (Carnot) efficiencies.

The maximum output power P_{max} and the efficiency η of the solar conversion of heat into electrical energy was measured on a series of four – leg thermoelectric oxide modules (TOM). The modules were constructed by combining two p- ($La_{1.98}Sr_{0.02}CuO_4$) and two n-type ($CaMn_{0.98}Nb_{0.02}O_3$) thermoelements connected electrically in series and thermally in parallel. The temperature gradient ΔT was applied by a High – Flux Solar Simulator source (HFSS) which generates a spectrum similar to solar radiation. The influence of the coating graphite layer on the hot side of the Al_2O_3 substrate compared to the uncoated surface on ΔT, P_{max} and η was studied. The measurements show an almost linear temperature profile along the thermoelectric legs. The maximum output power of 88.8 mW was reached for a TOM, with a leg length of 5 mm at ΔT = 622 K. The highest conversion efficiency η was found for a heat flux between 4 – 8 W cm^{-2} and the dependence of η on the leg length was investigated.

Project goals

The decrease of fossil fuels availability has motivated many research groups to find alternative energy sources [1, 2]. Solar cells operating at 20 % efficiency and covering 0.1% of the earth's land area would give enough energy to supply the yearly worldwide energy demand [3]. The sun as energy source can also be used by thermoelectric (TE) modules, which directly convert heat (i.e. solar heat) into electricity. The advantage of TE modules compared to solar cells is that TE modules utilize the IR and part of the UV and visible radiation of the solar spectrum while solar cells only uses the UV spectrum [4]..

The performance of a thermoelectric material is specified by the Figure of Merit, $ZT = S^2T / \rho\kappa$, where S is the Seebeck coefficient, ρ is the electrical resistivity and κ is the thermal conductivity. A sufficient conversion efficiency η requires values of the Figure of Merit of at least of $ZT \sim 1$. The conversion efficiency is thermodynamically limited by the Carnot efficiency [5]. As it was shown by Yang & Caillat, a Figure of Merit in the range of $2 < ZT < 3$ leads to a conversion efficiency of ~ 50 % of the Carnot efficiency. Beside the properties of the thermoelectric materials the conversion efficiency also depends on the construction of the TE device.

1. Thermoelectric modules

Commercial thermoelectric devices are based on Bi_2Te_3 because this material exhibits a relatively high Figure of Merit [6-7]. Disadvantage of Bi_2Te_3 are its limited chemical stability at high temperatures and its toxicity. Therefore, complex metal oxides are promising alternatives for high temperature applications because they are stable at high temperatures in air and non-toxic [8-12]. Among these oxides, $Na_xCo_2O_4$ [13] is especially interesting as it shows a high Figure of Merit, ZT ~ 0.8 at T = 800 K [14]. The production of single crystal material and keeping a stable stoichiometry is difficult, though In contrast, perovskite – type materials based on manganate and cuprate can be easily synthesized with controllable TE properties and relatively cost-effective. The demonstration of the direct conversion of solar heat into electrical energy by a series of thermoelectric modules based on perovskite-type oxide materials is crucial to enhance interest in thermoelectricity.

2. Novel thermoelectric materials

The TOM project aims at finding improved thermoelectric ceramics for the converters. Thus, several candidates were synthesised and characterised.

2.1. Sr1-xNaxRuO3

However, development and understanding of the properties of the new promising unconventional materials is the goal of the present and the future work. The studied $Sr_{1-x}Na_xRuO_3$ and $PrCo_{1-x}Ni_xO_3$ ceramics belong to a large perovskite-type family studied since the 1940s [15, 16]. Perovskite-type systems based on copper have been intensively investigated in the 1990s because of their superconducting behavior. The colossal magneto resistance effect (CMR) of manganites was subject of intensive research more recently [17, 18]. Studies on double perovskites e.g. investigating the spin polarized carriers in Sr_2FeMoO_6 or checking the Ru valence in $La_{2-x}Sr_xCoRuO_6$ were carried out during the last decade [19, 20]. Physical properties of 4*d* and 5*d* metal oxides still represent a less explored area of research, though.

The orthorhombic $SrRuO_3$ belongs to the perovskite-type family as well. It shows the *Pbnm* space group, metallic conductivity and ferromagnetic behavior below $T_C \sim 160$ K [21]. The itinerant character of the ferromagnetism in $SrRuO_3$ is underlined by unsaturated magnetization under the high magnetic field and the character of conducting electrons ranks this material to the family of strongly electron - correlated systems [22]. Considering the robustness of the metallic ground state of $SrRuO_3$ with respect to both electron occupancy and crystal lattice distortion, we studied the highly homogeneous and crystallographically well characterized $Sr_{1-x}Na_xRuO_3$ ($0.0 \leq x \leq 0.19$) ceramics in order to localize possible

magnetically polarized Ru 4*d* electrons when their density is decreased due to the charge compensation (Sr^{2+} <=> Na^{1+}).

2.2. $PrCo_{1-x}Ni_xO_3$

The spin state of Co^{3+} ions in perovskite-type cobaltates can be low-spin (LS, $t_{2g}^6 e_g^0$), intermediate-spin (IS, $t_{2g}^5 e_g^1$) and high-spin (HS, $t_{2g}^4 e_g^2$). This multitude of the spin states dramatically influences the physical properties associated with magnetic and electronic transitions. Simultaneous changes in the crystal structure along with Jahn-Teller distortion of the CoO_6 octahedron are observed [23-24]. The paramagnetic insulators $PrCoO_3$ and $LaCoO_3$ are isoelectronic. However, $LaCoO_3$, the most studied rare-earth cobalt perovskite, has a rhombohedral crystal structure in contrast to the orthorhombic $PrCoO_3$ due to the smaller ionic radius of the Pr^{3+} ion [26]. The substitution of Co by Ni influences the character of the electronic transport which changes from variable range hopping (VRH) into nearest neighbor hopping (NNH) [27]. The dependence of the Seebeck coefficient of the Ni substitution follows the Heikes equation [28]. Hashimoto et al. investigated a direct relationship between the ionic radii of rare-earth elements in perovskite-type Ln oxides and their thermoelectric properties [14]. The orthorhombic perovskite $PrCoO_3$ with the space group *Pbnm* shows insulator-like conductivity and paramagnetic behavior in the temperature range of 4 K < T < 1000 K with an effective magnetic moment μ_{eff} = 3.41 μ_B which is close to the effective magnetic moment of μ_{eff} = 3.58 μ_B for free Pr^{3+} ion [30, 31]. The electronic structure of $PrCoO_3$ shows a strong hybridization of the Pr 4*f* states with the O 2*p* and Co 3*d* valence electronic states with Co^{3+} in the IS state at T = 300 K. Below T = 300 K, an increase of the Co^{3+} LS state is observed suggesting a first Co^{3+} IS / Co^{3+} LS transition [32]. A LS-LS / HS-IS transition model based on specific heat measurements and spin entropy calculations was successfully applied to described the second spin state transition at ~ 600 K [33]. The crystal-field splitting of the Pr^{3+} *4f* multiplet as well as the Co ions in the higher spin state behaving as scattering centers for phonons adds to the reduction of the phonon thermal conductivity [34].

2.3. Cr – O – N

Transition metal nitrides show high chemical stability, resistance to corrosion and good mechanical properties [35], especially high hardness. The hardness of the solid solutions of $Cr_{1-x}Ti_xN$ strongly depends on the chemical composition. It increases with increasing Ti concentration. This is due to the growth of larger grains which leads to a decrease in electrical resistivity [36]. Transition metal nitrides exhibit relatively low electrical resistivities associated with a large Seebeck coefficient in case of CrN. Thus, CrN can be considered as a promising thermoelectric material [37]. CrN is the only mono-nitride that shows an antiferromagnetic-paramagnetic transition with a Neel temperature T_N ~ 273 K and a magnetic moment of 2.4 μ_B [38-40]. Below the magnetic ordering temperature T_N, the crystal structure transforms from cubic to orthorhombic. This change is due to the small distortion of the angle in the cubic structure [40]. The magnetic behavior of CrN is more complex as to the competition between the super-exchange (AFM) and double-exchange (FM) mechanism [41].

All the above-mentioned compounds could serve as potential thermoelectric materials. Hence, understanding the interrelation of their structural and physical properties is crucial in order to fine-tune and employ them in thermoelectric applications.

Experiments and results

1. Thermoelectric oxide modules (TOMs) applied in direct conversion of simulated solar radiation into electrical energy

A series of four leg perovskite thermoelectric oxide modules (TOMs) were tested for their ability to convert solar heat directly into electrical energy. The influence of the leg length, the emissivity of the absorber plate (graphite or SiC coating), and the heat flux on the maximum output power and the conversion efficiency was investigated.

A High-Flux Solar Simulator (HFSS) was used as heat source (Fig. 1a) [41]. A water-cooled, high-pressure argon arc lamp enclosed in a quartz shelter produces radiation in the visible, infrared and ultraviolet region of the spectrum. The power flux intensity and the temperature can be adjusted by varying the position of the target along the axis of the focusing mirrors or by changing the electrical input power at the arc electrodes. With the HFSS, flux intensities above 500 W cm^{-2} and temperatures exceeding 3000 K can be reached. The input heat fluxes (0 – 14.4 W cm^{-2}) were measured by a water cooled Thermogage Circular Foil Heat Flux Transducer TG1000-1 (Vatell Corporation) with a calibration range of 0 – 179 W cm^{-2}, a sensor sensitivity of 0.084 mV W^{-1} cm^{-2} and a sensor emissivity of 0.97.

A test unit with a data logger was used to measure the voltage in an open circuit mode and under load resistance. The test unit consisted of four resistances connected in parallel to yield 10 loads and a digital multimeter to measure the voltages. The measurements were monitored using the software LABVIEW. The output power was calculated from the voltage and load resistance values.

The bottom side of the TOMs was cooled by cold water circulating in a Cu block. TOMs were fixed to the Al-holder using a thermally conductive paste (DuPont™) in order to increase the heat transfer from the cold Al_2O_3 layer to the Al-holder. The Al-holder itself was placed on the Cu block cooling unit with a surface area of 50 x 50 mm^2 (Fig. 1b). A series of 0.5 mm thick K – type thermocouples was used to measure the temperature on the hot and cold side of the TOM as well as in the *p*- and *n*-type legs. One thermocouple was attached to the hot and cold Al_2O_3 absorber layer, respectively, and two to each TE leg by means of drilled holes with 0.6 mm in diameter (Fig. 1c). Typical measurement runs started by applying different heat fluxes until temperatures at the TOM showed steady state behavior. Simultaneously, the voltages in the open circuit mode, the load resistances and the temperatures on the hot and cold side of the TOMs and the Al_2O_3 substrates were recorded.

$La_{1.98}Sr_{0.02}CuO_4$ and $CaMn_{0.98}Nb_{0.02}O_3$ were used as p- and n-type materials with thermal conductivities of 2.5 W m^{-1} K^{-1} and 3 W m^{-1} K^{-1} above 300 K, respectively. The materials were hydrostatically pressed into pellets and showed 90% of the theoretical density without any crack formation due to the uniformly applied pressure. High density of the TE legs is the requirement for the production of mechanical stable TE modules. Thus, it is essential to find materials that combine a low thermal conductivity with a good mechanical stability.

In this study, we applied optimum materials with similar thermoelectric properties in order to build an efficient TOM. The electrical resistivity of both the *p*- and *n*-type legs show metallic behavior with a similar values of ρ_p = 24 mΩ cm and ρ_n = 20 mΩ cm, respectively, at T = 300 K. Both materials exhibit large thermopower (S_p = +200 µV K^{-1} and S_n = -160 µV K^{-1}, respectively) at T = 300 K.

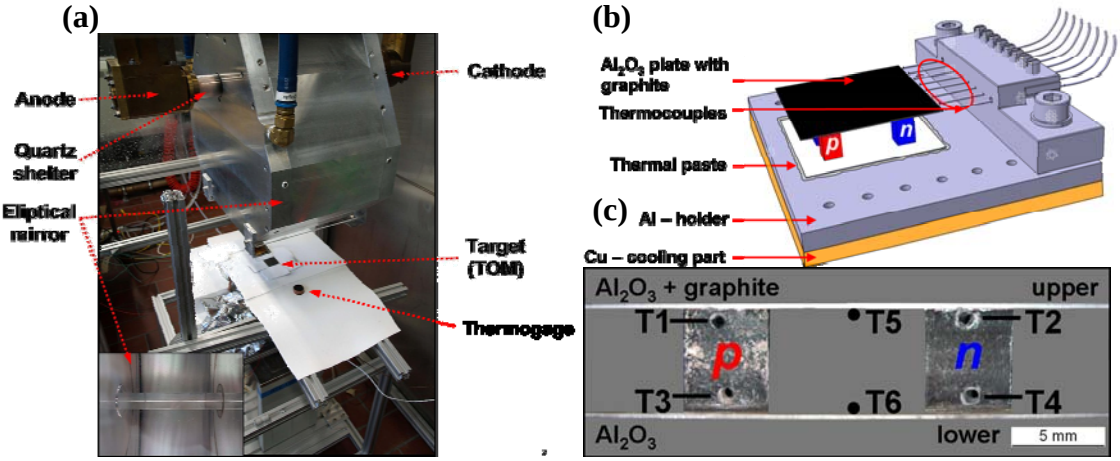

Fig. 1: (a) The High-Flux Solar Simulator at the ETH. An elliptical mirror redirects the radiant power of the enclosed argon arc lamp onto the target (TOM). (b) Sketch of a TOM testing unit mounted on the Al-holder for the thermocouples and the Cu-cooling part by thermal paste. The hot side of the Al_2O_3 substrate of the four - leg TOM is coated by a graphite layer. (c) Positions of the thermocouples in a cross-sectional profile of the 5mm TOM. 0.5 mm thick K-type thermocouples were placed in drilled holes.

Similar thermoelectric properties of the materials are a prerequisite for good conversion efficiencies of TE modules as previously described by G. Snyder et al. [42]. The compatibility factor *s*, defined as $s = [(1+ZT)^{-1/2}-1]/ST$, is used to assess the similarity of thermoelectric properties of different materials. While other thermoelectric parameters can change dramatically with temperature, the compatibility factor should not for maximum efficiency [42]. The closer the compatibility factors are for two materials, the higher the maximum efficiency of the thermoelectric module will be. The compatibility factor*s* of the two materials are perfectly matching around T = 425 K but, with increasing temperature, the ratio of the compatibility factors becomes 1.3 at T = 500 K and 2.3 at T = 800 K. Thus, the efficiency of the four – leg modules will be reduced at high temperatures.

In the temperature range of 300 – 450 K, the Figure of Merit *ZT* of the *p*-type material is higher than that of the *n*-type material due to its higher Seebeck coefficient. At T > 400 K, the *ZT* value of the *p*-type leg decreases as the Seebeck coefficient decreases (S ~ 130 µV K^{-1} at 800 K) while the *ZT* value of the *n*-type leg still increases due to S ~ -240 µV K^{-1}, resulting in ZT ~ 0.08 at T = 800 K.

The maximum temperature that can be applied when using a graphite-coated Al_2O_3 absorber plate is limited to T ~ 910 K where the graphite starts to sublimate. Sublimation would results in a decrease in temperature difference between the hot and cold side of the module as well as in a decrease in output power and conversion efficiency (Fig. 3). This is caused by the lower absorptivity of the Al_2O_3 absorber plate when the graphite coating vanishes. By increasing the heat flux, the temperature on the hot side of the module (*T5*) increases as expected. All the results are summarized in Table I. At the same heat flux, temperatures on the hot side of the *p*- and *n*-type TE legs (*T1*, *T2*) are comparable which means that the interconnection quality between the hot Al_2O_3 layer and the TE legs is equivalent. Inducing absolute temperatures > 400 K, temperatures on the cold side of the module are lower in the *p*-type leg (*T3*) than in the *n*-type leg (*T4*) due to a lower thermal conductivity of the *p*-type material.

On the cold side of the Al_2O_3 absorber plate (*T6*), temperatures are not equal which can be explained by a not sufficiently tight contact between the module and the Al-holder and deficiencies of the thermal paste. The difference amounts up to 140 K for the 4 mm TOM 1 and the 5 mm TOM 4. The 5 mm TOM 4 was coated with SiC (ε ~ 0.7; total spectrum measured) [43] so the lower temperature gradient compared to the graphite-coated 5 mm TOM 1 (ε ~ 0.95 – 0.97; total spectrum measured) [43] was expectable. The temperature gradient along the TE legs is almost linear. Above T = 400 K, temperature profiles of the *p*-type legs show lower values than of the *n*-type legs due to a higher thermal conductivity at this temperature. The temperature difference on the hot side of the Al_2O_3 absorber plate (*T5*) between the uncoated and the graphite-coated TOM is ~ 160 K for a heat flux of 9.5 W cm^{-2} as heat absorption is improved by a higher emissivity of the coated surface. Additionally, insufficient cooling on the cold side of the module leads to an increase in *T6* of 7 K.

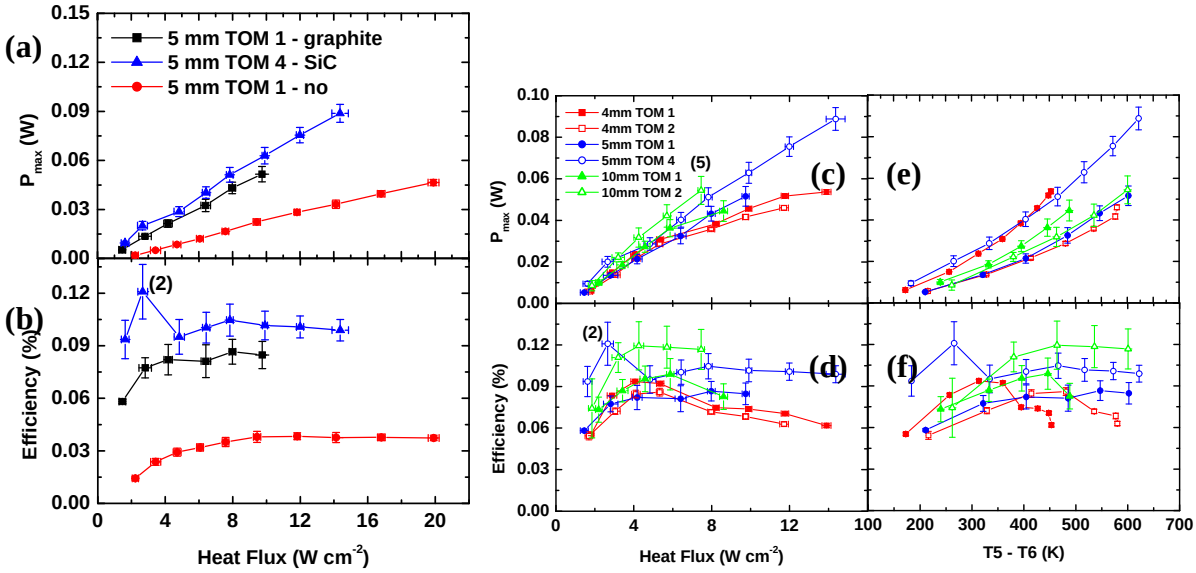

Fig. 2: (a) Maximum output power and (b) conversion efficiency as function of heat flux of 5 mm TOM 1 and 5 mm TOM 4. Maximum output power and conversion efficiency as a function of heat flux (c, d) and temperature difference between hot plate and cold plate, respectively (e, f).

Based on the voltage measurements in open-circuit mode (V_{oc}) and at load resistances, the maximum output power (P_{max}) was calculated considering the load resistance equal to the internal resistance [44]. P_{max} for 5 mm coated and uncoated TOMs is plotted in Fig. 2a. For the 5 mm TOM 1, P_{max} is higher for the graphite coated than for the uncoated module. At the same heat flux of ~ 9.5 W cm^{-2}, the temperature difference between *T5* and *T6* amounts to 602 K and 448 K for the graphite coated and the uncoated 5 mm TOM 1. Accordingly, an open circuit voltage V_{OC} of 44.6 mV (graphite-coated) and 31.7 mV (uncoated) was measured which results in values for P_{max} of 51.6 mW and 22.6 mW for the coated and uncoated 5 mm TOM, respectively. For the 5 mm SiC-coated TOM 4, V_{OC} = 38.3 mV, *T5* – *T6* = 507 K and P_{max} = 60.6 mW at a heat flux of ~ 9.5 W cm^{-2}. Despite the lower emissivity of SiC compared to graphite the 5 mm TOM 4 has a higher maximum output power P_{max} even though the open circuit-voltage V_{OC} is smaller. As the same *p*- and *n*-type materials are used for all the TOMs, this finding might only be due to small manufacturing deviations which could affect the contact resistances.

Knowing the input heat flux measured by the Thermogage, and the open-circuit voltage V_{oc} measured by a test unit with a data logger, we can calculate the conversion efficiency η, defined by:

$$\eta = \frac{V_{OC}^2}{4R_{load}\left(\frac{V_{OC}-V_{load}}{V_{load}}\right)Q_{in}}, \quad (1)$$

where V_{load} is the voltage at load resistance, R_{load} is the load resistance, and Q_{in} is the input heat flux on the surface of the Al_2O_3 absorber plate. Conversion efficiencies against heat flux for 5 mm TOMs are presented in Fig. 2b. The conversion efficiencies of the graphite-coated 5 mm TOM 1 and the SiC-coated TOM 4 are higher than the efficiency of the uncoated 5 mm TOM 1 which is in agreement with the P_{max} results. As for the 5 mm TOM 4, fluctuation of the η values (2nd point of the blue curve in Fig. 2b) was caused by a combination of radiation fluctuation (horizontal error bars) and the instability of V_{load} (vertical error bars). Fig. 2c-f summarize the data for P_{max} and η vs. heat flux and *T5* – *T6* for 4, 5 and 10 mm TOMs coated with graphite (5 mm TOM 4 coated with SiC). Depending on the temperature

difference *T5 – T6*, the maximum output power P_{max} increases exponentially and the maximum value of 54.4 mW was achieved for a leg length of 10 mm (5th point in Fig. 2e).

Table I: Summary of the properties of four – leg TOMs.

	$T5_{max}$ [K]	$T6_{max}$ [K]	ΔT [K]	ε [const.]	$Q_{in, max}$ [W cm^{-2}]	$V_{OC, max}$ [mV]	η [%]	P_{max} [mW]	$Q_{in, opt}$ [W cm^{-2}]	η_{max} [%]
4 mm TOM 1	913	460	453	~ 0.95	13.90	42.9	0.062	53.7	4.06	0.094
4 mm TOM 2	926	346	580	~ 0.95	11.72	39.4	0.063	46.1	5.33	0.086
5 mm TOM 1	915	313	602	~ 0.95	9.75	44.5	0.085	51.6	7.98	0.087
5 mm TOM 4 *	941	319	622	~ 0.70	14.37	46.4	0.099	88.8	7.83	0.105
10 mm TOM 1	901	412	489	~ 0.95	8.61	45.3	0.083	44.5	5.87	0.099
10 mm TOM 2	964	363	601	~ 0.95	7.46	52.4	0.117	54.4	4.26	0.119

$T5_{max}$ and $T6_{max}$ are the maximum temperatures reached by applying the maximum input heat flux $Q_{in, max}$.

$V_{OC, max}$, η and P_{max} are the maximum open circuit voltage, efficiency and maximum output power, respectively, reached by applying $Q_{in, max}$.

$Q_{in, opt}$ is the optimum input heat flux in order to reach the maximum conversion efficiency η_{max}.

* Coated by SiC.

Depending on the heat flux, the maximum output power of 88.8 mW was obtained for the 5 mm TOM 4 at a heat flux of 14.4 W cm^{-2} and a temperature difference of *T5 – T6* = 622 K. Theoretically, the highest P_{max} value would be expected for a 10 mm TOM. However, sublimation of the graphite coating at high temperatures (caused by heat fluxes exceeding 7.5 W cm^{-2}) leads to lower values.

The maximum conversion efficiency of 0.12 % was obtained for a TOM with 10 mm leg length and an Al_2O_3 absorber area of 25 x 25 mm^2 (Fig. 2d, f). Taking an absorber surface area equivalent to the area of the *p*- and *n*-type legs as a basis, the maximum conversion efficiency will reach ~ 1 %. The conversion efficiency is higher at higher heat fluxes resulting in higher temperature differences *T5 – T6* which improves the Carnot efficiency. However, at higher temperatures and higher heat fluxes the emissivity of the Al_2O_3 absorber plate increases with T^4. Thus, the conversion efficiency reaches an optimum value after which it decreases. The optimum conversion efficiency for 4 mm TOMs is around 4 W cm^{-2}, for 5 mm TOMs between 4 – 8 W cm^{-2} and for 10 mm TOMs around 6 W cm^{-2}.

2. Physical properties of $Sr_{1-x}Na_xRuO_3$ (x = 0 – 0.19)

The morphology of the $Sr_{1-x}Na_xRuO_3$ (x = 0 – 0.19) samples was determined by Scanning Electron Microscopy (SEM) and is shown in Fig. 3. The ceramic samples are composed of particles with average sizes between 50 – 1500 nm. We found that samples with x = 0.09 and x = 0.16 are made up of large crystallites while the samples with x = 0.0 and especially with x = 0.19 consist of grains with a dispersion down to ~ 50 nm. In general, smaller grains improve the material's electrical conductivity. Thus, a lower resistivity for samples with x = 0.0 and x = 0.19 compared to samples with x = 0.09 and x = 0.16 can be expected. In fact, the lowest resistivity is observed for the sample with x = 0.19 (Fig. 4). This is likely due to the favorable morphology of the ceramic sample containing mostly fine grains which embed a small amount of large crystallites (Fig. 3e). These crystallites where surveyed by electron

microprobe and an unexpected high Na concentration was measured (Fig. 3f). Energy dispersive X-ray (EDX) analysis identified the needle-shaped impurity phase to be the insulating hexagonal perovskite Sr_3NaRuO_6 [45].

All the solid solutions of the $Sr_{1-x}Na_xRuO_3$ system have orthorhombic crystal structure and belong to the *Pbnm* space group. The ratio of the cell parameters $a > c/\sqrt{2} > b$ is valid for all Na-doped compounds. The lattice parameters are linearly decreasing with increasing Na substitution on the A-site which is due to the lower ionic radius of Na ($r_{Na+} < r_{Sr2+}$). Consequently, all the samples of $Sr_{1-x}Na_xRuO_3$ (x = 0.0 - 0.19) have a Goldschmidt tolerance factor $t < 1$ which decreases with increasing x while a small orthorhombic distortion remains constant at ~ 0.43 ± 0.04 %. The Ru – O bond length slightly decreases with increasing Na content and the valence bond angle Ru – O – Ru varies between 163 – 164 °. The valence bond angle differs from the ideal cubic angle because of the cooperative rotation of the RuO_6 octahedra in $SrRuO_3$.

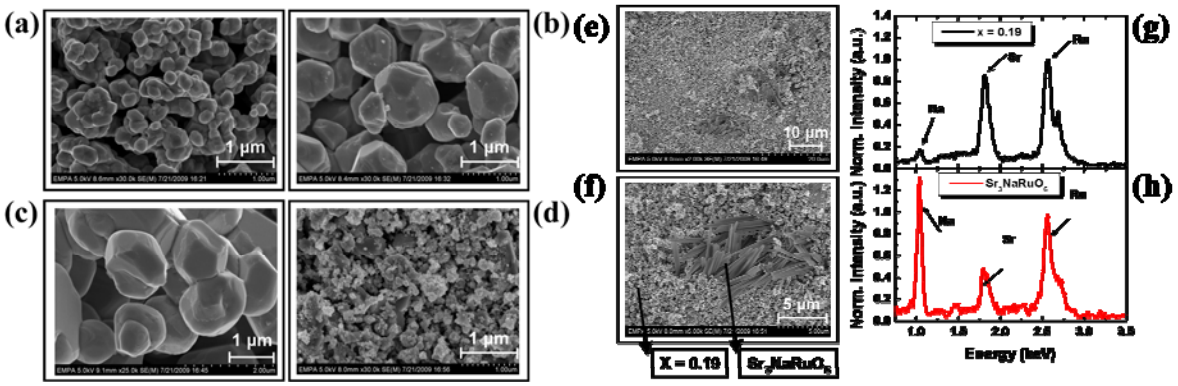

Fig. 3: SEM pictures of the samples with (a) x = 0.0, (b) x = 0.09, (c) x = 0.16, (d) x = 0.19. SEM pictures of the sample (e, f) x = 0.19 and EDX spectra of the (g) x = 0.19 and the (h) impurity phase of Sr_3NaRuO_6.

The temperature dependence of the thermal and electrical properties is shown in Fig. 4. The total thermal conductivity in this temperature range, composed of the electronic and phononic part according to $\kappa_{total} = \kappa_{el} + \kappa_{ph}$, increases with increasing temperature. At room temperature, values are in the range of 1.5 to 2.8 W m^{-1} K^{-1}. The electronic part κ_{el} can be roughly estimated using the Wiedemann - Franz law, $\kappa_{el} = L_0 \sigma T$, where $L_0 = 2.443\ 10^{-8}$ W S^{-1} K^{-2} is the Lorenz number for free electron gas, σ is the electrical conductivity, and T is the absolute temperature. Consequentially, the phononic part can be obtained and is shown in the inset. As depicted, the phonon thermal conductivity κ_{ph}, is varying between 1.3 and 1.7 W m^{-1} K^{-1} at 300 K. This indicates that regardless a strong scattering of phonons on other phonons, grain boundaries and defects there could be a significant coupling between phonons and spin excitations. Consequently, the character of the magnetic transition at T_C is not purely of the 2nd order but also involves, at least to a small extend, the lattice degree of freedom via spin – lattice coupling.

The temperature dependence of the Seebeck coefficient and the electrical resistivity is plotted in Fig. 4b - c, respectively. All the samples show metallic behavior with $d\rho / dT > 0$. The resistivity values at 300 K vary between 0.75 to 16.3 mΩcm and predominantly depend on the morphology and microstructure of the ceramic sample. As expected, the sample with x = 0.19 exhibits the best metallicity which is likely due to the small grain size.

The Seebeck coefficient S for all samples, shown in Fig. 4b, is positive in the whole temperature range indicating the dominant role of holes in the electronic conduction mechanism. The high temperature Seebeck coefficients approach constant values between 31 and 36 µV K^{-1} at 300 K. The change of the slope at T_C is likely associated with the change of spin entropy which may contribute to the Seebeck coefficient at high temperatures [47]. The almost linear temperature dependence of the Seebeck coefficient at low temperatures

(inset of Fig. 4b) reflects the metallicity of all the samples. The high *S* / *T* slope *is in* agreement with a high Sommerfeld coefficient *γ* (varying between 30.9 mJ mol^{-1} K^{-2} (x = 0.0) to 43 mJ mol^{-1} K^{-2} (x = 0.19)) as Behnia et al. stated that, the *S* / *T* ratio and *γ* increase simultaneously with increasing x [48].

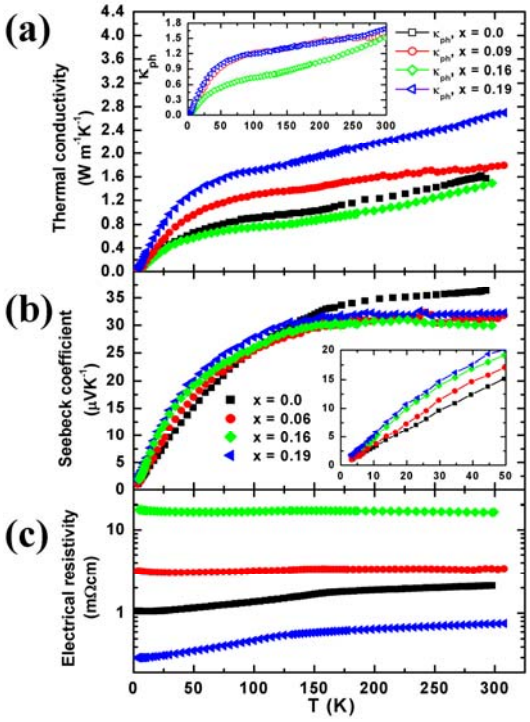

Fig. 4.: (a) Temperature dependence of the total and the phononic (inset) thermal conductivity (κ_{total} and κ_{ph}), (b) the Seebeck coefficient and (c) the electrical resistivity for $Sr_{1-x}Na_xRuO_3$ (0.0 < x < 0.19).

3. $PrCo_{1-x}Ni_xO_3$: Crystal structure, magnetic and transport properties

All the $PrCo_{1-x}Ni_xO_{3\pm\delta}$ (0.0 < x < 0.62) phases have orthorhombic crystal structure with *Pbnm* space group. The refined lattice parameters increase with increasing Ni content. The ratio $a > c/\sqrt{2} > b$ is valid for all Ni-doped compounds. The Seebeck coefficient, thermal conductivity and electrical resistivity in the temperature range of 3.5 K < T < 300 K were measured on bar shaped pellets with theoretical densities of ~ 92 % for the sample with x = 0.62 and of ~ 65 % for all other samples. The temperature dependence of the electrical resistivity is plotted in Fig. 5a. The samples with 0.0 ≤ x ≤ 0.29 show insulating behavior with $d\rho / dT < 0$ whereas the samples with 0.49 ≤ x ≤ 0.62 show semiconducting to metallic behavior. The resistivity values at 300 K vary between 2.4 10^4 and 8.3 mΩcm. The activation energy E_a defined as $E_a = k_B \cdot d(\ln \rho) / d(1/T)$, derived from the Arrhenius law ($\rho(T) = \rho\infty \exp(E_a / k_B T)$), gives values of 560 meV, 400 meV, 270 meV and 430 meV for x = 0.07; 0.29, 0.49 and 0.62, respectively, at T = 300 K (inset of Fig. 6a). The activation energy of the samples with 0.07 < x < 0.29 shows unlinear behavior in the temperature range of 5 K < T < 300 K. For the sample with x = 0.07 the activation energy reaches the maximum at T = 115 K with E_a = 550 meV followed by the energy minimum at T = 230 K. The sample with x = 0.29 has an activation maximum at T = 280 K and in the temperature range of 120 K < T < 185 K the activation energy approaches a constant value E_a = 380 meV.

The Seebeck coefficient *S*, shown in Fig. 5b, is positive for the samples with 0.0 < x < 0.51 in the whole temperature range indicating the dominant role of holes in the electronic conduction mechanism. The high temperature Seebeck coefficient decreases from 836 μV K^{-1} for x = 0.0 to 12 μV K^{-1} for x = 0.51 at 300 K. Only the Seebeck coefficient of

$PrCo_{0.38}Ni_{0.62}O_3$ exhibits negative values indicating the dominant role of electrons in the electronic conduction mechanism. The observed Seebeck coefficient S_{300K} = 258 μV K^{-1} for x = 0.07 provides an estimate of n_h = 0.049 / M when the classical Heikes formula for the Seebeck coefficient $S_{h,e} = \pm(k/e)\ln\left[(1-n_{h,e})/n_{h,e}\right]$ is applied for hole *h* and electron *e* charge carriers, respectively. Similarly, the observed Seebeck coefficient S_{300K} = 72 μV K^{-1}, 12 μV K^{-1} and -16 μV K^{-1} provide estimates of n_h = 0.302 / M, 0.465 / M and n_e = 0.546 for x = 0.29, 0.49 and 0.62, respectively.

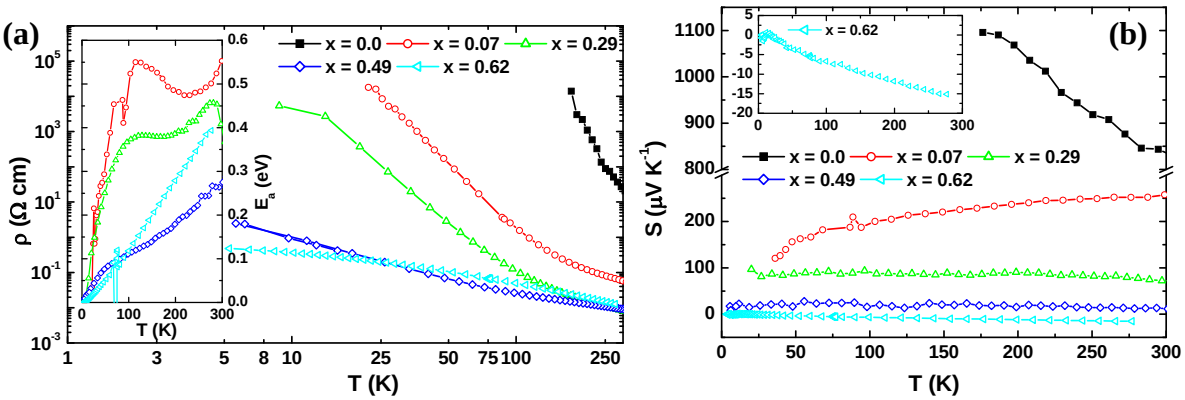

Fig. 5: (a) Temperature dependence of the electrical resistivity for $PrCo_{1-x}Ni_xO_{3\pm\delta}$ (0.0 < x < 0.62) with the inset of the activation energy defined as $E_a = k_B \cdot d(\ln\rho)/d(1/T)$. (b) Temperature dependence of the Seebeck coefficient; the inset shows the temperature dependence of the Seebeck coefficient of $PrCo_{0.38}Ni_{0.62}O_3$.

The total thermal conductivity, κ_{total}, of Ni-doped $PrCoO_3$ increases with increasing temperature. The phononic part of the thermal conductivity predominates with κ_{ph} > 92 % of the total thermal conductivity. The unusual behavior of the thermal conductivity of $PrCoO_3$ has a three temperature region. A sudden decrease of the thermal conductivity above T = 23 K from κ_{total} = 6.55 W m^{-1} K^{-1} to 3.38 W m^{-1} K^{-1} at T = 73 K is attributed to phonon – phonon umklapp scattering becoming dominant in this temperature range. In the intermediate temperature region of 73 K < T < 175 K the thermal conductivity increases from 3.38 W m^{-1} K^{-1} to 3.79 W m^{-1} K^{-1}due to crystal-field splitting between the ground state and first excited level of the Pr^{3+} *4f* shell. A second decrease of the thermal conductivity between 175 K and 294 K is caused by additional phonon scattering due to the spin state transition [24].

The magnetic susceptibility of Ni-doped $PrCoO_3$, was measured in a zero-field-cooled (ZFC) and a field-cooled (FC) regime applying a magnetic field of 0.1 T. The ZFC and FC curves differed considerably which is typical for spin glass materials. With increasing x the effective magnetic moment, determined in the low temperature range of 100 K < T < 150 K based on the Curie –Weiss law , increases up to μ_{eff} = 0.75 μ_B for x = 0.29 and then decreases to μ_{eff} = 0.65 μ_B for x = 0.92. The Weiss constant increases with increasing Ni concentration from Θ = -50 K for x = 0.0 to Θ = 44 K for x = 0.29 and subsequently decreases to Θ = 22 K for x = 0.62. implying that the ferromagnetic interactions are weaker at higher Ni concentrations. These results are in agreement with the electrical transport behavior as the transition between insulating and the semiconducting to metallic behavior was observed at Ni contents between 0.29 and 0.49.

The oxidation state of the Co ions was studied by X-ray absorption near-edge structure (XANES)[*]. The edge position scarcely changes by Ni substitution and for all the samples the nominal oxidation state remains as Co^{3+}. As the Ni content increases, there is a subtle shift of the edge position (ΔE = - 0.6 eV from x = 0.0 to x = 0.62) to lower energies. Also, a reduction of the white line intensity (very small effect) with increasing Ni substitution is observed. Finally, a reduction of the pre-edge intensity can be noticed as the Co content decreases. The pre-edge feature A comes from a quadrupole *1s→3d* transition, which is

dipole forbidden. However, the Co-*3d* band is strongly hybridized with the O-*2p* state, providing a *p*-character to the band. These findings, although they could indicate a slight reduction of the Co oxidation state from Co^{3+} to $Co^{3-\delta}$ with decreasing Co content, are so small that they can be explained by geometrical effects. On the other hand, the Ni *K*-edge position slightly shifts to higher energies (ΔE = + 0.5 eV from x = 0.07 to x = 0.62) as the Co content decreases (Ni content increases from x = 0.07 to x = 0.62),. However, as in the case of the Co *K*-edge, the nominal oxidation state of the Ni cations is Ni^{3+} in all the samples. A small increase of the intensity of the Ni pre-edge peak with increasing Ni content is observed, too. As stated above, this is rather due to a geometrical effect than to a change in the Ni oxidation state from $Ni^{3-\delta}$ to Ni^{3+} (accompanying a supposed change in the Co oxidation state).

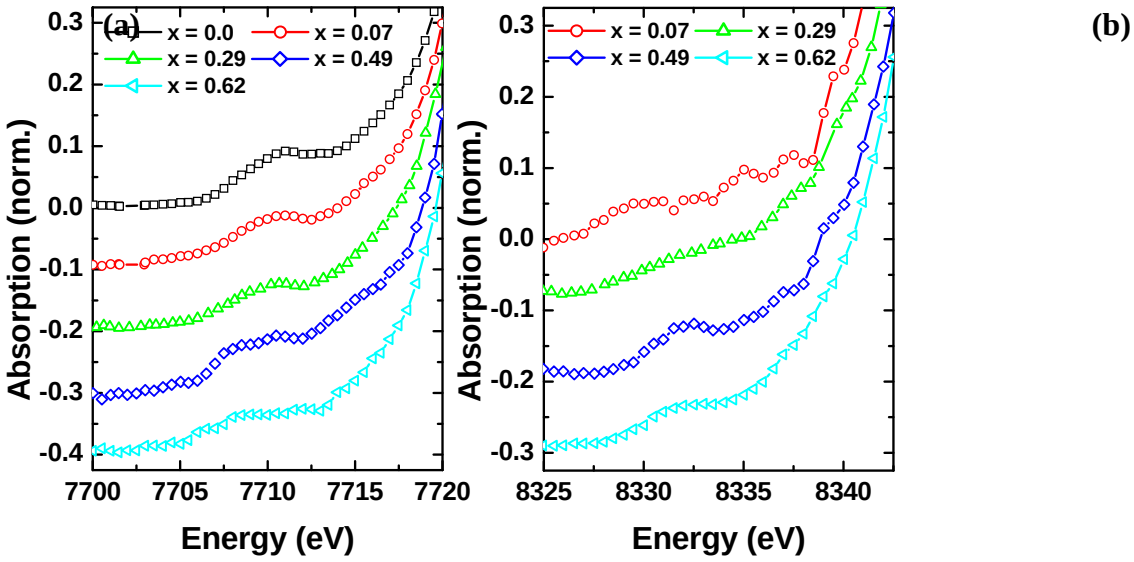

Fig. 6: Pre-edge region of the XANES spectra at the Co *K*-edge and Ni *K*-edge (left and right diagram, respectively) for $PrCo_{1-x}Ni_xO_{3\pm\delta}$ (0.0 < x < 0.62).

However, the important decrease in the intensity of the pre-edge peak cannot be explained by reduction from Co^{3+} to $Co^{3-\delta}$. Figures 6 a-b show the change of the pre-edge peaks of the Co and Ni *K*-edges for different Ni contents. It can be observed that with increasing Ni substitution, the intensity of both the Co and Ni pre-edges diminish and even broaden. Moreover, for $PrCo_{0.9}Ni_{0.1}O_3$, no pre-edge in the Ni *K*-edge spectrum can be distinguished. This might be due to the weakening of the Co *3d* – O *2p* hybridization as a consequence of the substitution of Co by Ni. Due to the different relative energy levels of the *3d* band of Co and Ni with respect to the Fermi level (since Ni has one electron more) the O *2p* orbitals spread to cover both *3d* states to form the antibonding *p-d* hybridization with the M-absorber and the M cations at the 3rd coordination sphere. This spreading of the *p-d* hybridized state around the Fermi level results in a broadening and a pre-edge intensity reduction.

4. The physical properties of Cr – O – N

It was determined that CrN has a cubic crystal structure with *Fm-3m* space group and a lattice parameter a = 4.1506(2) Å. The refinement of the XRD data is plotted in the left diagram of Fig. 7. The inset in Fig. 7 shows the unit cell of the perovskite-type crystal structure of Cr – O – N. The atomic percent ratio of 0.09 for oxygen which replace the nitrogen was measured by hot gas extraction so that the nominal composition of the sample is $CrO_{0.09(3)}N_{0.90(7)}$. This composition was considered for the Rietveld refinement of the crystal structure. The TGA / DTA measurement was performed in order to estimate the temperature

stability of the sample. The observed mass increase above T ~ 700 K was due to oxidation of $CrO_{0.09(3)}N_{0.90(7)}$. This stability limit is much better than that of conventional thermoelectric modules based on Bi_2Te_3 which operate far below 700 K because of their low temperature stability. Figures 7 a-d show TEM diffractograms, conventional images and high resolution images of the Cr – O - N sample. Fig. 7a represents the diffraction pattern and the indexing which is in agreement with the atomic model obtained by Rietveld refinement. The particle size is ranging from 30 to 150 nm and particles mainly have polygonal shapes (see the detail of the size and morphologies of the Cr – O - N particles in Fig. 7b - c). Similar particle sizes between 10 and 50 nm were also found by Inumaru et al. [50]. Due to the small particle size the electrical resistivity is reduced to 2.8 mΩcm at room temperature (see below). The high resolution image of one particle shown in Fig. 7d corresponds to zone axis and confirms the good crystallinity of the sample [36, 38, 39, 49-55].

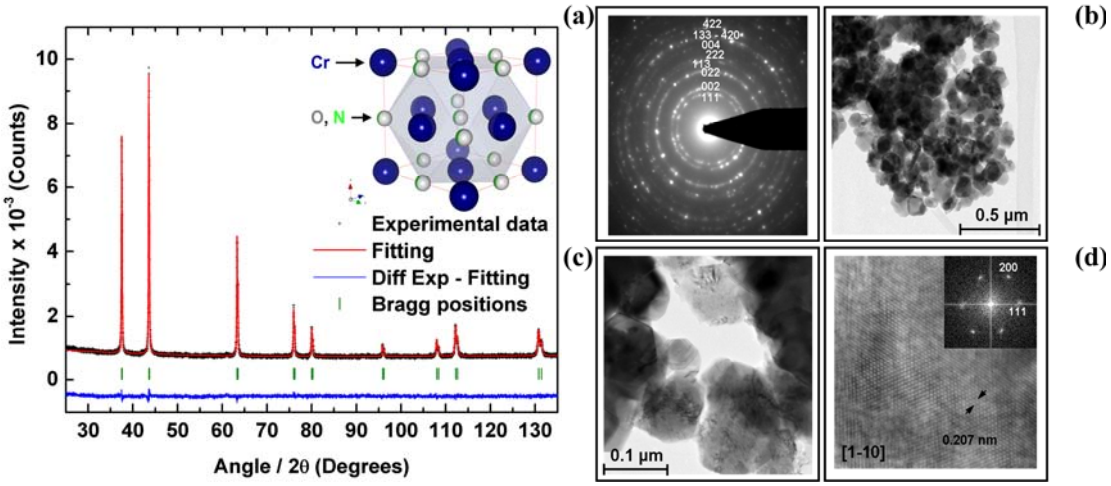

Fig. 7: (Left diagram) Rietveld refinement of the X-ray powder diffraction data for $CrO_{0.09(3)}N_{0.90(7)}$. Space group: Fm-3m. The observed intensities, calculated profile, difference curve and Bragg positions are shown. The inset shows the picture of the cubic perovskite-type crystal structure of $CrO_{0.09(3)}N_{0.90(7)}$. (Right diagram) (a) Diffraction pattern and indexing which is in agreement with the atomic model obtained by Rietveld refinement, (b, c) detail of the size and morphology of the Cr – O - N particles and (d) high resolution image of one particle which corresponds to the [1-10] zone axis and confirms the good crystallinity of the sample.

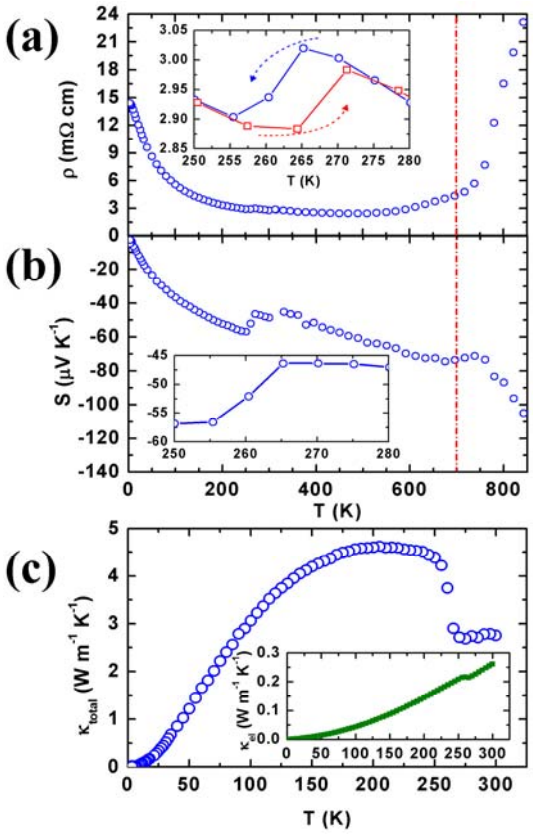

Fig. 8: (a) Temperature dependence of the electrical resistivity with the zoom around T_C during the cooling and heating, (b) Seebeck coefficient and (c) thermal conductivity with the inset showing the electronic contribution (κ_{el}) to total thermal conductivity of Cr – O - N.

The temperature dependence of the electrical resistivity and Seebeck coefficient, *S,* between 3 K < T < 850 K are plotted in Fig. 8 a-b. The inset of Fig. 8a shows the hysteresis of the electrical resistivity measurement during the cooling and heating. This hysteresis was reported by several research groups [38] and is associated with a structural phase transition. The low electrical resistivity of ~ 2.8 mΩcm at T = 300 K reflects the metallic Such a low value was also measured for $Cr_{0.9}V_{0.1}N$ by Quintela et al. [37]. They reported the systematical gradual suppressing of the electrical resistivity by increasing the vanadium content in the CrN matrix.

The Seebeck coefficient of the sample is negative, indicating that the main charge carriers are electrons, and linearly decreasing with temperature which is typical for metallike compounds. Between 255 K and 265 K, *S* drops from -56 μV K^{-1} to -46 μV K^{-} and at T = 300 K S = -48 μV K^{-1}. The Seebeck coefficient of the $CrO_{0.09(3)}N_{0.90(7)}$ is smaller compare with the $Cr_{0.9}V_{0.1}N$ (S = -83 μV K^{-1} at T = 300 K), though [37]. The low electrical resistivity and $|S|$ > 100 μV K^{-1} result in a power factor *PF*, defined as PF = S^2 / ρ, of ~ 1.7 10^{-4} W K^{-2} m^{-1} at T = 590 K. Due to much higher Seebeck coefficients,, higher PF values of ~ 2.0 10^{-4} W K^{-2} m^{-1} and 3.0 10^{-4} W K^{-2} m^{-1} are reported for $Cr_{0.95}V_{0.05}N$ and $Cr_{0.9}V_{0.1}N$, respectively [37].

The bulk sample density is 60 % of the theoretical density. Total thermal conductivity composed of an electronic and phononic part $\kappa_{total} = \kappa_{el} + \kappa_{ph}$ is plotted in Fig. 8c. The thermal conductivity increases with increasing temperature indicating metallic behavior and between 255 K < T < 265 K κ_{total} it decreased by about 35 % from 4.2 $Wm^{-1}K^{-1}$ to 2.7 $Wm^{-1}K^{-1}$. Since, κ_{ph} makes the main contribution to the total thermal conductivity κ_{total} of $CrO_{0.09(3)}N_{0.90(7)}$, the phononic part has to be decreased in order to be interesting for possible future thermoelectric applications.

National collaborations

- A. Bitschi, High Voltage Laboratory, Swiss Federal Institute of Technology, Physikstrasse 3, 8092 Zurich, Switzerland.
- C. Suter, Institute of Energy Technology, ETH Zurich, Sonneggstrasse 3, 8092 Zurich, Switzerland.
- D. Logvinovich, École Polytechnique Fédérale de Lausanne, Laboratoire de Cristallographie, BSP, CH-1015 Lausanne, Switzerland

International collaborations

- J. Hejtmánek, Institute of Physics of ASCR, v.v.i, Laboratory of oxide materials, Na Slovance 2, 182 21 Praha 8, Czech Republic.
- E. Šantavá, Institute of Physics of ASCR, v.v.i, Department of low temperatures, Na Slovance 2, 182 21 Praha 8, Czech Republic.
- F. J. Villacorta, SpLine / Spanish CRG beamline (BM25), European Synchrotron Radiation Facility, F-38043 Grenoble CEDEX, France.
- R. Robert, Grey Solid State Chem. Res. Group, Department of Chemistry SUNY at Stony Brook, USA.

Conclusions for 2009 and outlook 2010

A four - leg thermoelectric oxide module combining *p*- and *n*-type thermoelements made of and $CaMn_{0.98}Nb_{0.02}O_3$, respectively, was successfully used to directly convert simulated solar radiation using a HFSS as energy source into electrical energy. The Figure of Merit ZT of the *p*- and *n*-type thermoelectric materials was evaluated up to 800 K showing nearly constant values at higher temperatures for the *p*-type and a linear increase with temperature up to ZT = 0.08 for the *n*-type material. The electrical resistivity of both materials shows metallic behavior with ρ between 20 - 24 mΩ cm at T = 300 K and $|S| \geq 160$ μV K^{-1} at T = 300 K. The temperature gradient along the TE legs was almost linear showing a lower value for the *p*-type legs compared to the *n*-type legs due to higher thermal conductivity of $La_{1.98}Sr_{0.02}CuO_4$ above T = 400 K. It was shown that coating of the hot side of the Al_2O_3 absorber plate by graphite induced a larger temperature gradient in the TOMs and the maximum output power and conversion efficiency was significantly improved. A heat flux between 4 – 8 W cm^{-2} resulted in the highest conversion efficiency. The maximum conversion efficiency of 0.12 % was obtained for a TOM with 10 mm leg length and based on an $_{absorber}$ area equivalent to the area of the TE legs, the conversion efficiency would even be ~ 1 %.

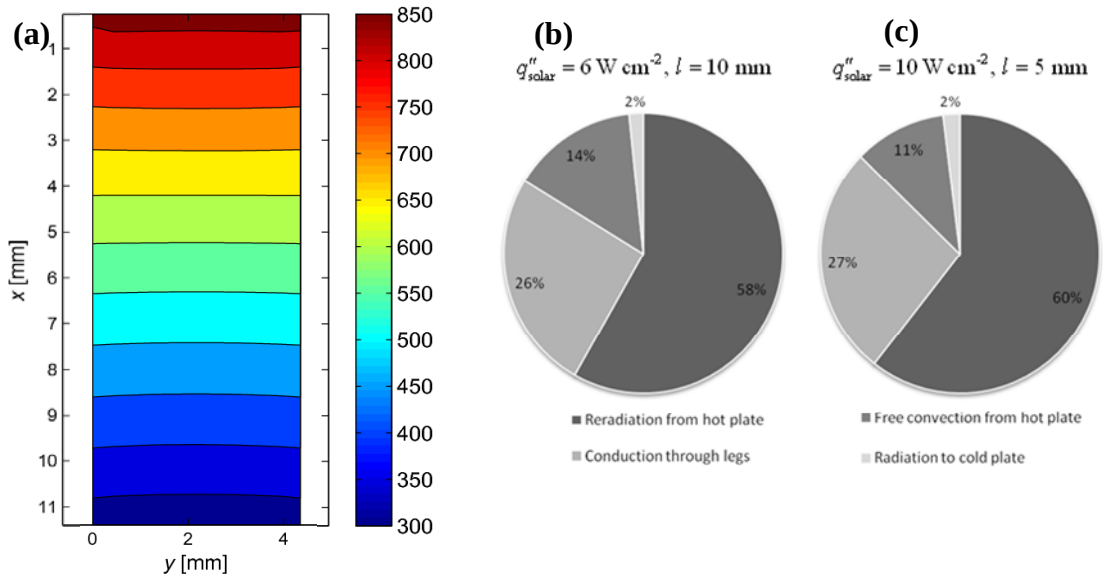

Fig. 9: (a) Temperature profile along the 10 mm length of p-type ($La_{1.98}Sr_{0.02}CuO_4$) leg at a heat flux of 6 W cm^{-2}. (b) Analysis of the heat transfer mode through the 10 mm TOM by applying the heat flux of 6 W cm^{-2} and through the (c) 5 mm TOM at a heat flux of 10 W cm^{-2}.

The radiation as well as the heat conduction in the module itself were determined by theoretical calculations of C. Suter, ETH, based on the thermoelectric properties of the *p*- and *n*-type materials and the absorber plate, assuming the boundary conditions of a fixed temperature on the cold side of the TOM, constant diffuse solar flux from the solar source, no local convection and working at open circuit voltage (j = 0, V = 0). From Figure 9 is evident, that the temperature distribution along the *p*-type leg linear. The analysis of the heat transfer through the 5 mm and 10 mm TOM is shown in Fig. 9 b-c. The analysis suggests that only ~ 25 % of the input heat is conducted through the TOM, approximately 70 % is lost due to either radiation or free convection and about 2 % are lost due to radiation to the Al_2O_3 absorber plate on the cold side of the TOM.

A tomography-based computational analysis using SLS synchrotron radiation was adopted to design and optimize the thermoelectric modules in regard an efficient electrical power production[**]. A high-quality tomography of the materials is required in order to yield their detailed microstructure, which in turn is needed for calculating the effective transport properties. The exact geometrical 3D configuration of complex porous materials is obtained by high resolution computer tomography, digitalized, and used to calculate the morphological and transport characteristics by direct pore level simulations of the momentum and energy conservation equations.

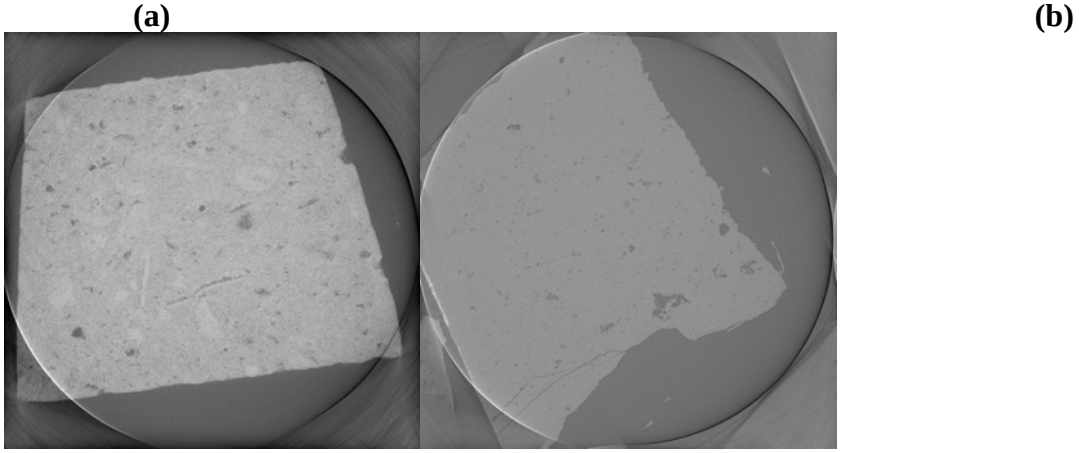

Fig. 10: (a) 2D High resolution tomography image of the p-type ($La_{1.98}Sr_{0.02}CuO_4$) and (b) n-type ($CaMn_{0.98}Nb_{0.02}O_3$) leg.

First preliminary results obtained by FT analysis are shown in Fig. 10. From the whole 3D picture of the *p*- and *n*-type legs we are able to gain a better understanding of the heat transfer processes in the TOM. Calculations include morphological properties (e.g., porosity, specific surface area), conduction transfer properties (e.g. thermal/electric conductivity), radiation heat transfer properties (e.g., extinction coefficient; scattering phase function, scattering albedo), and fluid flow properties (e.g., Dupuit-Forchheimer coefficient, permeability, interfacial heat transfer coefficient, dispersion tensor, residence time, tortuosity).

The development of the new thermoelectric materials requires the understanding of the fundamental mechanisms of thermoelectricity. So, basic studies will continue to be a part of our future work. Thereby, we hope to find an efficient thermoelectric material to be implemented in TE devices, where we extend our knowledge each year. The following publications about material properties and solar experiments with TOMs are in progress:

- C. Suter, P. Tomeš, M. Trottmann, A. Weidenkaff, and A. Steinfeld, Heat transfer analysis and optimization of thermoelectric converters driven by concentrated solar radiation (2009/2010).
- D. Logvinovich, A. Arakcheeva, P. Pattison, S. Eliseeva, P. Tomeš, I. Marozau, and G. Chapuis, Crystal structure, optical and magnetic properties of $Pr_2(MoO4)_3$ (2009/2010).
- P. Tomeš, C. Suter. M. Trottmann, M. H. Aguirre, P. Haueter, A. Steinfeld, and A. Weidenkaff, Thermoelectric oxide modules (TOMs) applied in direct conversion of simulated solar radiation into electrical energy (2009/2010).
- P. Tomeš, D. Logvinovich, J. Hejtmánek, M. H. Aguirre, A. Weidenkaff, On the physical properties of Cr – O – N (2009/2010).
- P. Tomeš, R. Robert, F. J. Villacorta, J. Hejtmánek, A. Weidenkaff, On the $PrCo_{1-x}Ni_xO_3$: Crystal structure, magnetic and transport properties (2009/2010).

References

[1] Alternative energy sources, V.P.M.'s Polytechnic, Thane (2005).

[2] A. Steinfeld, *Sol. Energy* **78**, 603 (2005).

[3] R. A. Meyers, *Encyclopedia of Physical Science & Technology* **15**, 237 (2001).

[4] T. M. Tritt, H. Böttner, and L. Chen, *MRS Bulletin* **33**, (2008).

[5] J. Yang, T. Caillat, *MRS Bulletin* **31**, 224 (2008).

[6] S. S. Kim, F. Yin, Y. Kagawa, *J. Alloys Compd.* **419**, 306 (2006).

[7] O. Yamashita, S. Tomiyoshi, K. Makita, *J. Mater. Sci.* **40**, 6439 (2005).

[8] E. S. Reddy, J.G. Noudem, S. Hebert and C. Goupil, *J. Phys. D: Appl. Phys.* **38**, 3751 (2005).

[9] W. Shin, N. Muruyama, K. Ikeda and S. Sago, *J. Power Sources* **103**, 80 (2001).

[10] R. Funahashi, M. Mikami, T. Mihara, S. Urata and N. Ando, *J. Appl. Phys.* **99**, 066117 (2006).

[11] R. Funahashi, I. Matsubara, H. Ikuta, T. Takeuchi. U. Mizutani and S. Sodeoka, *Japan. J. Appl. Phys.* **39**, L1127 (2000).

[12] R. Funahashi, S. Urata, K. Mizuno, T. Kouuchi and K. Mikami, *Appl. Phys. Lett.* **85**, 1036 (2004).

[13] I. Terasaki, Y. Sasago and K. Uchinokura, Phys. Rev. B 56, R12685 (1997).

[14] M. Ito**,** T. Nagira, D. Furumoto, S. Katsuyama and H. Nagai, *Scr. Mater.* **48**, 403 (2003).

[15] G. Cao, S. McCall, M. Shepard, J. E. Crow, R. P. Guertin, *Phys. Rev. B* **56**, 321 (1997).

[16] M. T. Anderson, K. B. Greenwood, G. A. Taylor, K. R. Poeppelmeier, *Prog. Solid State Chem.* **22**, 197 (1993).

[17] K. Chahara, T. Ohno, M. Kasai, Y. Kozono, *Appl. Phys. Lett.* **63**, 1990 (1993).

[18] Z. Jirák, J. Hejtmánek, K. Knížek, R. Sonntag, *J. Solid State Chem.* **132**, 98 (1997).

[19] P. Tomeš, J. Hejtmánek, K. Knížek, *Solid State Sci.* **10**, 486 (2008).

[20] K. L. Kobayashi, T. Kimura, H. Sawada, K. Terakura, Y. Tokura, *Nature* **395**, 677 (1998).

[21] X. - Y. Zhang, Y. Chen, Z. - Y Li, C. Vittoria, V. G. Harris, *J. Phys.: Condens. Matter* **19**, 266211 (2007).

[22] L. Klein, J. S. Dodge, C. H. Ahn, G. J. Snyder, T. H. Geballe, M. R. Beasley, A. Kapitulnik, *Phys. Rev. Lett.* **77**, 2774 (1996).

[23] S. K. Pandey, A. Kumar, S. Khalid and A. V. Pimpale, *J. Phys.: Condens. Matter* **18**, 7103 (2006).

[24] K. Knížek, Z. Jirák, J. Hejtmánek, P. Novák, *J. Phys.: Condens. Matter* **18**, 3285 (2006).

[25] K. Knížek, Z. Jirák, J. Hejtmánek, M. Veverka, M. Maryško, G. Maris, T. T. M. Palstra, *Eur. Phys. J. B* **47**, 213 (2005).

[26] J.-Q. Yan, J.-S. Zhou, J. B. Goodenough, *Phys. Rev. B* **69**, 144409 (2004).

[27] T. Wu, G. Wu, X. H. Chen, *Solid State Commun.* **145**, 293 (2008).

[28] R. Robert, M. H. Aguirre, L. Bocher, M. Trottmann, S. Heiroth, T. Lippert, M. Döbeli, A. Weidenkaff, *Solid State Sci.* **10**, 502 (2008).

[29] H. Hashimoto, T. Kusunose, T. Sekino, *J. Alloys Compd.* **xxx**, xxx (2009).

[30] K. Sekizawa, M. Kitagawa, Y. Takano, *J. Magn. Magn. Mater.* **177**, 541 (1998).

[31] I. G. Deac, R. Tetean, I. Balasz, E. Burzo, *J. Magn. Magn. Mater.* **xxx**, xxx (2009).

[32] S. K. Pandey, S. Patil, V. R. R. Medicherla, R. S. Singh, K. Maiti, *Phys. Rev. B* **77**, 115137 (2008).

[33] K. Knížek, J. Hejtmánek, Z. Jirák, P. Tomeš, P. Henry, G. André, *Phys. Rev. B* **79**, 134103 (2009).

[34] K. Berggold, M. Kriener, P. Becker, M. Benomar, M. Reuther, C. Zobel, T. Lorenz, *Phys. Rev. B* **78**, 134402 (2008).

[35] G. C. A. M. Janssen, F. D. Tichelaar, C. C. G. Visser, *J. Appl. Phys*. **100**, 093512 (2006).

[36] X. Jin, L. Gao, J. Sun, *Acta Mater*. **54**, 4035 (2006).

[37] C. X. Quintela, F. Rivadulla, J. Rivas, *Appl. Phys. Lett*. **94**, 152103 (2009).

[38] J. D. Browne, P. R. Liddell, R. Street, and T. Mills, *Phys. Status Solidi A* **1**, 715 (1970).

[39] A. Mavromaras, S. Matar, B. Siberchicot, G. Demazeau, *J. Magn. Magn. Mater*. **134**, 34 (1994).

[40] L. M. Corliss, N. Elliott, J. M. Hastings, *Phys. Rev*. **117**, 4 (1960).

[41] D. Hirsch, P. v. Zedtwitz, and T. Osinga, *J. Sol.Energy Eng.* **125**, 117 (2003).

[42] G. J. Snyder, *Appl. Phys. Lett.* **84**, 2436 (2004).

[43] M. A. Bramson, Infrared radiation – A handbook of applications, (1968).

[44] P. Tomeš, R. Robert, M. Trottmann, L. Bocher, M. H. Aguirre, J. Hejtmánek and A. Weidenkaff, submitted *J. Electron. Mater.*, (2009).

[45] J. Darriet, F. Grasset, P. D. Battle, *Mater. Res. Bull.* **32**, 139 (1997).

[46] B. Dabrowski, O. Chmaissem, P. W. Klamut, S. Kolesnik, M. Maxwell, J. Mais, Y. Ito, *Phys. Rev. B* **70**, 014423 (2005).

[47] Y. Klein, S. Hebert, A. Maignan, S. Kolesnik, T. Maxwell, B. Dabrowski, *Phys. Rev. B* **73**, 052412 (2006).

[48] K. Behnia, D. Jaccard, J. J. Flouquet, *Phys. Condens. Matter* **16**, 5187 (2004).

[49] W.J. Feng, D. Li, W.F. Li, S. Ma, Y.B. Li, D.K. Xiong, W.S. Zhang, Z.D. Zhang, *J. Alloys Compd*. **425**, 4 (2006).

[50] K. Inumaru, K. Koyama, Y. Miyaki, K. Tanaka, and S. Yamanaka, *Appl. Phys. Lett*. **91**, 152501 (2007).

[51] K. Suzuki, T. Kaneko, H. Yoshida, H. Morita, H. Fujimori, *J. Alloys Compd*. **224**, 232 (1995).

[52] M. S. Miao, P. Lukashev, A. Herwadkar, and W. R.L. Lambrecht, *Phys. Status Solidi C* **7**, 2516 (2005).

[53] K. Suzuki, H. Morita, T. Kaneko, H. Yoshida and H. Fujimora, *J. Alloys Compd*. **201**, 11 (1993).

[54] K. Suzukia, T. Kanekob, H. Yoshida, Y. Obi, H. Fujimori, H. Morita, *J. Alloys Compd*. **306**, 66 (2000).

[55] E. Fawcett, *Rev. Mod. Phys*. **60**, (1988).

Appendix

List of conference contributions and scientific publications in 2009

SCI Publications:

- K. Knížek, J. Hejtmánek, Z. Jirák, P. Tomeš, P. Henry, G. André, Neutron diffraction and heat capacity studies of $PrCoO_3$ and $NdCoO_3$, *Phys. Rev. B* **79**, 134103 (2009).
- Logvinovich, D. J. Hejtmánek, M. Maryško, N. Homazava, P. Tomes, S.G. Ebbinghaus, A. Reller, and A .Weidenkaff, On the magnetic properties of $SrMoO_2N$, *J. Appl. Phys,* 105 (2009) 023522.
- Tomes, P., Robert, R. Trottmann, M., Bocher, L., Aguirre, M. H., Hejtmanek, J., and Weidenkaff, A. Perovskite-type thermoelectric oxide modules (TOM) for electric power generation, *J. Electr. Mat.* accepted.
- Suter, C., Tomeš, P., Steinfeld, A. and Weidenkaff, A., Heat Transfer Analysis and Geometrical Optimization of Thermoelectric Converters Driven by Concentrated Solar Radiation, *Materials*, in press.
- Tomes, P., Knizek K., Weidenkaff ., and Hejtmanek J., On the physical properties of $Sr_{1-x}Na_xRuO_3$ (x = 0 – 0.19), *JSSC*, accepted.

Conferences:

- Swiss Workshop on Materials with Novel Electronic Properties Manep, Thermodynamic, magnetic and transport properties on FM Sr1-xNaxRuO3 with respect to weak localization effects, Les Diablerets, 2009. (poster)
- 28th International Conference on Thermoelectrics and 7th European Conference on Thermoelectrics, Thermoelectric and magnetic properties of $PrCo_{1-x}Ni_xO_3$ (x = 0.0 – 0.7), Freiburg 2009. (talk)
- 2nd Thermopower Symposium CH – 2009: Novel Thermoelectric Materials and Applications, Direct conversion of simulated solar radiation into electrical energy by thermoelectric oxide modules (TOM), Duebendorf 2009 (organisation committee). (poster)
- 33rd International Conference & Exposition on Advanced Ceramics & Composites, Thermoelectric and magnetic properties of $Sr_{1-x}Na_xRuO_3$ (x = 0 – 0.25), Daytona Beach 2009. (talk)

Proposals:

- * Valence shift and coordination environment of Co ions in $Pr_{1-x}Sr_xCoO_3$ as function of temperature (ID: CH/2762 BM25A 31-10-2008/04-11-2008, ESRF, Grenoble, Beamline BM25A, 30.10.2008 – 4.11.2008).
- ** Tomography-based determination of the effective transport properties of multiphase materials for solar-driven thermochemical and thermoelectrical processes (ID: 20090143, PSI – SLS, Beamline TOMCAT, 09.10.2009 – 10.10.2009).